Estimating the Response of Extreme Precipitation over Midlatitude Mountains to Global Warming

XIAOMING SHI AND DALE R. DURRAN

Department of Atmospheric Sciences, University of Washington, Seattle, Washington

(Manuscript received 3 November 2014, in final form 24 February 2015)

ABSTRACT

Global warming–induced changes in extreme orographic precipitation are investigated using a hierarchy of models: a global climate model, a limited-area weather forecast model, and a linear mountain wave model. The authors consider precipitation changes over an idealized north–south midlatitude mountain barrier at the western margin of an otherwise flat continent. The intensities of the extreme events on the western slopes increase by approximately 4% K^{-1} of surface warming, close to the ''thermodynamic'' sensitivity of vertically integrated condensation in those events due to temperature variations when vertical motions stay constant. In contrast, the intensities of extreme events on the eastern mountain slopes increase at about 6% K^{-1}. This higher sensitivity is due to enhanced ascent during the eastern-slope events, which can be explained in terms of linear mountain wave theory as arising from global warming–induced changes in the upper-tropospheric static stability and the tropopause level. Similar changes to these two parameters also occur for the western-slope events, but the cross-mountain flow is much stronger in those events; as a consequence, linear theory predicts no increase in the western-slope vertical velocities. Extreme western-slope events tend to occur in winter, whereas those on the eastern side are most common in summer. Doubling CO_2 not only increases the precipitation, but during extreme western slope events it shifts much of the precipitation from snow to rain, potentially increasing the risk of heavy runoff and flooding.

1. Introduction

In contrast to the global warming–induced changes in mean precipitation predicted by climate models, which decrease in certain regions such as the subtropics, precipitation extremes are expected to increase in almost all areas of the globe (Emori and Brown 2005; Kharin et al. 2007). Extratropical precipitation extremes in climate simulations increase at about 6% K^{-1} of globally averaged surface warming. This rate of increase is close to the ''thermodynamic'' sensitivity of condensation to warming, which is produced by temperature increases at fixed relative humidity when vertical motions stay almost constant (O'Gorman and Schneider 2009a). The simulated sensitivity of tropical precipitation extremes differs substantially between climate models. Nevertheless, by applying observational constraints to climate simulations and exploiting the relationship between the simulated responses to interannual variability and climate change, O'Gorman (2012) estimated a sensitivity of the 99.9th percentile of daily tropical precipitation to climate change at 10% K^{-1}.

With 26% of the world's population living within mountains or their foothills, and over 40% living in river basins originating in mountainous regions (Beniston 2005), understanding the response of orographic precipitation extremes to global warming is important for anticipating societal impacts such as flooding and landslides (Maddox et al. 1978; Lin et al. 2001; Rasmussen and Houze 2012). Yet only a few previous studies have reported on warming-induced precipitation extremes over mountains as part of more widely targeted numerical simulations. These studies (Diffenbaugh et al. 2005; Singh et al. 2013; Wehner 2013) suggest that precipitation extremes will increase in frequency and intensity over the high elevations and rain-shadowed regions of the Pacific Northwest region of the United States.

Here we use a combination of global climate and mesoscale weather forecast models, together with a linear mountain wave model, to develop a more complete physical understanding of the processes governing

---

Corresponding author address: Xiaoming Shi, Box 351640, Department of Atmospheric Sciences, University of Washington, Seattle, WA 98195.
E-mail: shixm@atmos.washington.edu

DOI: 10.1175/JCLI-D-14-00750.1

changes in extreme precipitation over simplified topography representative of one of the north–south mountain ranges along the west coast of North America. We use the mesoscale model to provide more detailed simulations of the response of midlatitude orographic precipitation extremes to global warming in the different environmental parameter regimes produced by the global climate model. The changes on both the windward (western) side of the mountains and their leeward (eastern) side are partitioned into the contributions from thermodynamics and from dynamics in the spirit of O'Gorman and Schneider (2009a,b). The linear mountain wave model is used to explore the physical principles governing the dynamical response.

The paper is organized as follows. Section 2 describes the numerical models used in our idealized experiments. Section 3 documents responses of the climatological means of orographic precipitation to doubled CO_2. Section 4 examines the distribution and synoptic-scale structure of the extreme events. The relative contributions of thermodynamics and dynamics to the changes in extreme-event intensity are explored in section 5. Section 6 examines the elevational dependence of the changes in extreme precipitation. Our conclusions are presented in section 7.

2. Models and methods

The numerical models used in our study are the Geophysical Fluid Dynamics Laboratory (GFDL) global High Resolution Atmospheric Model (HiRAM) (Zhao et al. 2009) and the Weather Research and Forecasting (WRF) Model, version 3.5.1 (Skamarock et al. 2008). The HiRAM model is run at approximately 50-km horizontal resolution to effectively create a multidecadal dataset for both a control and a globally warmed climate. The most extreme orographic precipitation events from this larger sample are dynamically downscaled using WRF at 12-km horizontal resolution.

To isolate the dynamic and thermodynamic processes governing the changes in extreme orographic precipitation, we consider an idealization of the mountainous terrain in North America, along with the drier plains to their east. Four copies of these prototypical North American continents are distributed at 90° intervals around the northern midlatitudes (Fig. 1a). The remainder of the planet is covered with a 24-m-deep mixed layer ocean. The continents extend 30° east–west in longitude and span the latitude band 30°–60°N. They are flat except on their west coasts, where a single smooth mountain ridge runs north–south just inland from the coast. The surface elevation z_s of each ridge is determined by

$$z_s(x,y) = \frac{h_m}{2}\begin{cases} 1+\cos(\pi r), & \text{if} \quad |r| < 1, \\ 0, & \text{otherwise}, \end{cases} \tag{1}$$

where $h_m = 2.5\,\text{km}$ is the height of the ridge[1] and $r(x, y)$ is defined as

$$r(x,y) = \begin{cases} \sqrt{\dfrac{(x-x_0)^2}{a^2}}, & \text{if} \quad |y-y_0| < b-a, \\ \sqrt{\dfrac{(x-x_0)^2 + [|y-y_0| - (b-a)]^2}{a^2}}, & \text{otherwise}; \end{cases} \tag{2}$$

here a is the east–west half-width of the ridge (set to 240 km in the HiRAM and 120 km in the WRF simulations), b is the north–south half-width (taken as 1675 km, corresponding to 15° in latitude, for all simulations), and x_0 and y_0 are the coordinates of the center of the ridge.

HiRAM has a finite-volume dynamical core using a cubed-sphere grid topology and sophisticated physics modules for simulating processes such as in cloud microphysics, moist convection, and land surface exchanges. The same model parameters and resolution (~50 km horizontally, 32 vertical levels) as those specified in Zhao et al. (2009) are adopted in our simulations. We run HiRAM with modern (330 ppm) and doubled (660 ppm) CO_2 concentrations and daily averaged solar insolation for 20 years, and retain 6-hourly data from the last 10 years for analysis. Since four identical continents are symmetrically distributed around a latitude circle, we treat the 10 years of global analysis data as a 40-yr dataset over a single continent. Our focus is precipitation on each side of the ridge on the western edge of this continent. The sensitivity of precipitation to global warming, for both time means and extremes, is defined as the percentage change in precipitation rate

---

[1] This is roughly the average height of Rocky Mountains (see Fig. 8a).

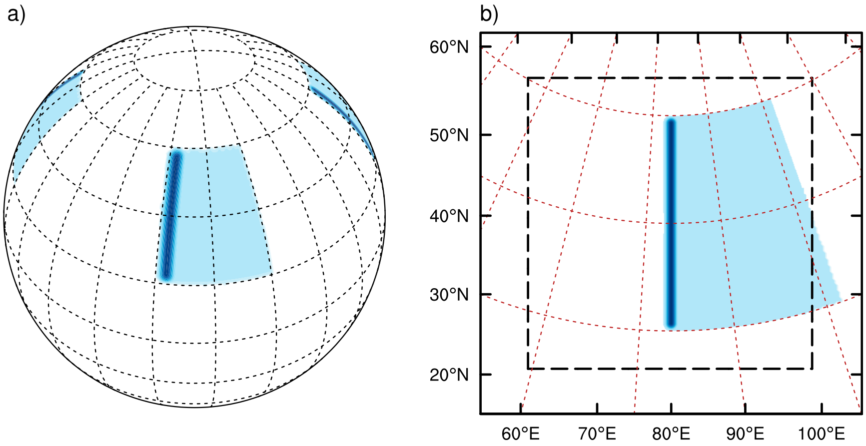

FIG. 1. Horizontal domains for the (a) HiRAM and (b) WRF simulations. In both panels, the blue shaded regions represent the continents, with the mountain ridge in darker blue. The dashed-line box in (b) is the lateral boundary of the inner (12 km) nested domain. (Cross sections of the mountain ridge are shown in Fig. 10.)

divided by the global mean surface temperature increase, which is 5 K is our simulations.

To select a group of extreme events over the mountains from each simulation, we need first identify individual precipitation events and define their intensities. Different events can be separated based on connectivity in latitude–time plots of the zonally averaged precipitation rate over each east–west segment of grid cells ascending the western or descending the eastern slopes. The latitude–time plots are smoothed by applying a four-point (24 h) running average in time and a three-point (150 km) running average in latitude before measuring connectivity. Each event identified in this way corresponds to an individual weather system passing over the mountains, and its intensity is defined as the mean precipitation rate in the 24 h and the 150-km-wide north–south latitude band on the eastern or western slope receiving the most precipitation during that event. Finally, all precipitation events over the eastern and over the western mountain slopes are ranked based on their intensities, and for each side of the ridge the top 40 events in the control and 2 × CO_2 simulations are selected for further analysis. Since a significant fraction of the air is diverted laterally around the northern and southern ends of the mountains, leading to different dynamical regimes in those regions, our analysis is restricted the segment of mountains between 32.5° and 57.5°N.

To attain a more robust evaluation of the changes in extreme events, the top 10 events in each 40-event set of HiRAM extremes are resimulated with WRF using higher resolution and narrower mountains whose slopes better approximate average slopes in the real world. The WRF simulations also use 18 more vertical levels than in HiRAM. In the WRF simulations, a 12-km resolution domain is one-way nested in a 36-km domain, whose initial and lateral boundary conditions are provided by the HiRAM data (Fig. 1b). The diurnal cycle is included in the WRF simulations, with the insolation determined by the calendar date of each individual event. The HiRAM fields are computed using daily averaged solar insolation; since the boundary of the outer WRF domain is entirely over the ocean, this did not lead to any incompatibilities. A list of the WRF physics schemes used in our simulations is provided in the appendix. The WRF simulations run for 5–6 days centered around the time of the HiRAM event. The time, location, and intensity of the most intense 24-h period in the finescale WRF run is determined in a manner similar to that for the parent HiRAM event except that the event precipitation is meridionally averaged over a 108-km (9 cell) latitude band.

Because of its higher resolution and superior microphysical parameterization, the WRF simulations provide better dynamical details of the extreme events than do HiRAM results. Nevertheless, the responses of the extreme events to warming are quantitatively consistent in all major aspects in the WRF and HiRAM simulations. Unless otherwise stated, we use data from WRF simulations for the discussion about extreme events in sections 4–6.

3. Responses of climatological means

Before examining the extremes, we briefly consider annual mean and seasonal mean orographic precipitation, and its response to increased CO_2 in the full

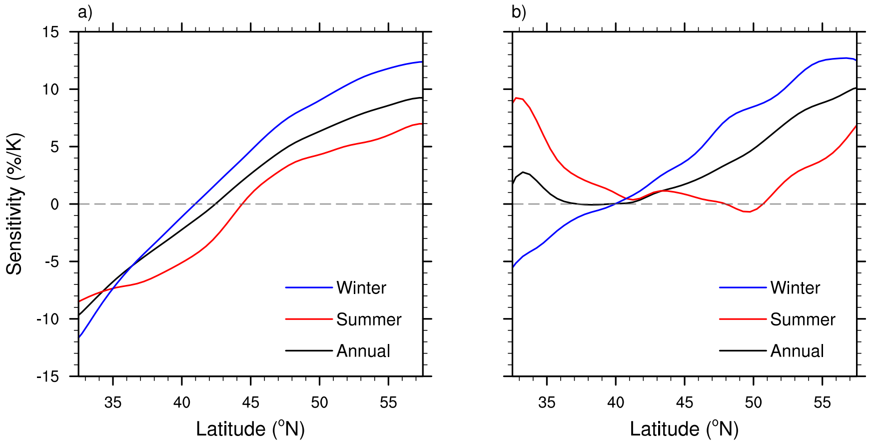

FIG. 2. Sensitivity of annual, summer, and winter mean precipitation over the (a) western and (b) eastern slopes of the mountains.

HiRAM dataset. For both the eastern and western slopes (halves) of the mountains, the annual and the seasonal mean precipitation are greatest over the center section of the ridge, and decrease to the north and south. Over the western slopes, the mean wintertime precipitation (December–February) is roughly twice that in summer (June–August), whereas the opposite is true over the eastern slopes.

Figure 2 shows the sensitivity to doubled CO_2 of the annual, summer, and winter mean precipitation over the western and eastern slopes of the mountains. The annual and seasonal mean western-slope precipitation sensitivities increase near the northern end of the mountains, decrease near the southern end, and vary smoothly with latitude in between (Fig. 2a). The wintertime western-slope sensitivities are more positive than those for the summertime and the annual mean, except near the southern end of the range. Shi and Durran (2014) conducted similar GCM simulations with annual mean insolation and a shallower slab ocean, and they found that the sensitivity of western-slope orographic precipitation varies from -9% to $13\%\,K^{-1}$ between 35° and 60°N, which is very close to the sensitivity of wintertime western-slope precipitation in our current simulations. Their analysis showed that the changes in the western-slope precipitation are produced by an almost spatially uniform thermodynamic increase resulting from the change in the lapse rate of saturation specific humidity and by a north–south asymmetry in dynamical changes produced by the poleward shift of storm tracks.

The sensitivity of the eastern-slope precipitation differs from that for the western slope in that there is increasing summertime precipitation over the southern part of the mountain despite the poleward shift of storm track. Since significant precipitation is likely associated with some sort of eddy, one might expect the eastern-slope precipitation to respond to warming in a manner similar to the summertime pattern over the western slope, because both of them are affected by the same storm track shift.

To understand why the sensitivity of the eastern-slope precipitation in summer does not have the expected north–south asymmetry, we composite the 850-hPa level wind fields for significant summer precipitation events over the eastern slope within the red square at 35°N shown in Fig. 3. Here "significant events" are taken as those times when 6-h precipitation rates averaged within the square are greater than $0.2\,mm\,h^{-1}$. About 9% of the total summertime period is taken up by these events, and they produce nearly ¾ of the total summertime rainfall.

Figure 3 compares the composite flow pattern for significant eastern-slope summertime events in the control and doubled-CO_2 simulations. Unlike wintertime, when significant eastern-slope precipitation occurs downstream of the axis of an open trough, significant summertime precipitation events occur when a small low to the south produces easterly upslope flow into the target area. This easterly upslope flow at 35°N is weaker in the doubled-CO_2 composite. As a consequence, the thermodynamic tendency toward increased precipitation is almost cancelled by weaker dynamical forcing, and the net sensitivity *per significant event* only increases by $0.8\%\,K^{-1}$. The actual increase in significant event precipitation is primarily as a result of a $3.3\%\,K^{-1}$ increase in the frequency of these events, which results from the weakening of climatological mean westerlies as the storm track shift poleward. The remainder of the weaker summertime events behave in a similar way, with the sensitivities produced by changes in frequency

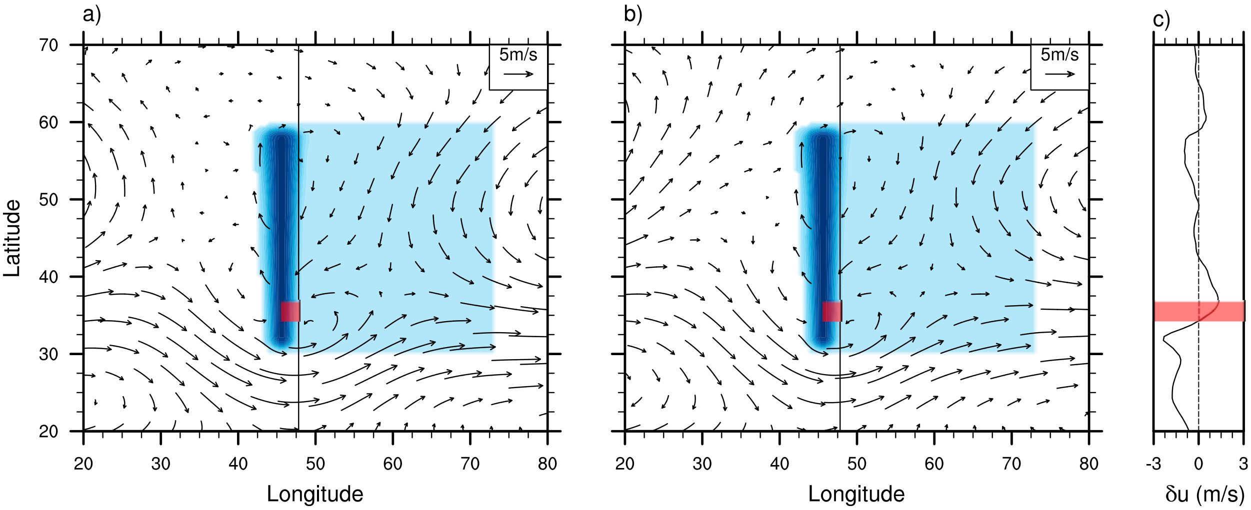

FIG. 3. Mean summertime 850-hPa level wind fields for "significant" precipitation events in the red box (see text) in the (a) control and (b) doubled-CO_2 climates. (c) The change in zonal wind due to warming at the longitude indicated by vertical black lines in (a),(b). Blue shaded region shows the continent, with the mountain ridge in darker blue.

and intensity for all events adding up to give a total sensitivity of about 6% K^{-1} at 35°N. In contrast the frequency of significant eastern-slope wintertime events is reduced by $-5.8\%\ K^{-1}$, consistent with a northward shift in storminess. This reduction is a major factor, but not the only contributor to the net climatological decrease of about $-3\%\ K^{-1}$ in the wintertime precipitation over the eastern slope in the south.

4. Distribution and synoptic structure of the extreme events

We now return the focus to extreme events, beginning with the four sets of top 40 events (western side, eastern side, control, and doubled CO_2) from the HiRAM simulations.

a. Location and frequency

The north–south distribution of 40 most extreme (99.75th percentile) west-side and east-side events from the HiRAM simulation are shown in Fig. 4, in which the latitude of the row of grid cells along the mountain slope receiving the maximum 24-h precipitation is binned in 2.5°-wide latitude bands along the length of the topography. Extreme events occur most frequently over the central part of the mountain range.

The mean latitude at which the western-slope extremes occur shifts northward by 0.9° in the doubled-CO_2 simulation, while the mean latitude for the eastern-slope extremes shifts southward by 1.1°. The northward shift in the western-slope events might be linked to the northward shift in the storm track in the warmer world (Yin 2005). Nevertheless, with only 40 events in our sample, the north–south distribution of these events is noisy. Applying the Kolmogorov–Smirnov test (Miller 1956; Marsaglia et al. 2003) to a null hypothesis that the latitudinal distribution of extremes shown in Fig. 4 does not change in the warmer climate, we found the hypothesis of no change could not be rejected at the 5% significance level.

The precipitation thresholds that distinguish the 10 and the 40 most extreme events in the control climate are exceeded far more frequently in the doubled-CO_2 simulation. Table 1 shows that on both the western and eastern slopes, the number of events that exceed the control climate 40-event threshold increases by about a factor of 3 in the doubled-CO_2 simulations. For just those events above the top 10 threshold, the increase in the warmer climate is more than a factor of 4.

b. Synoptic-scale structure

Western-slope and eastern-slope precipitation extremes tend to occur at different times in a year. As shown in Fig. 5, western-slope extremes mostly occur in winter months, whereas eastern-slope extremes are more likely to occur in the warm season. Figure 6 shows snapshots of water vapor path (WVP; the column integrated water vapor) and geopotential height at 500 hPa in a western-slope and an eastern-slope event. Although they are from individual cases, the synoptic patterns in Fig. 6 are very typical of the most extreme events in both the control and doubled-CO_2 climates. Unless specified otherwise, the data for this and the subsequent discussions are taken from the sets

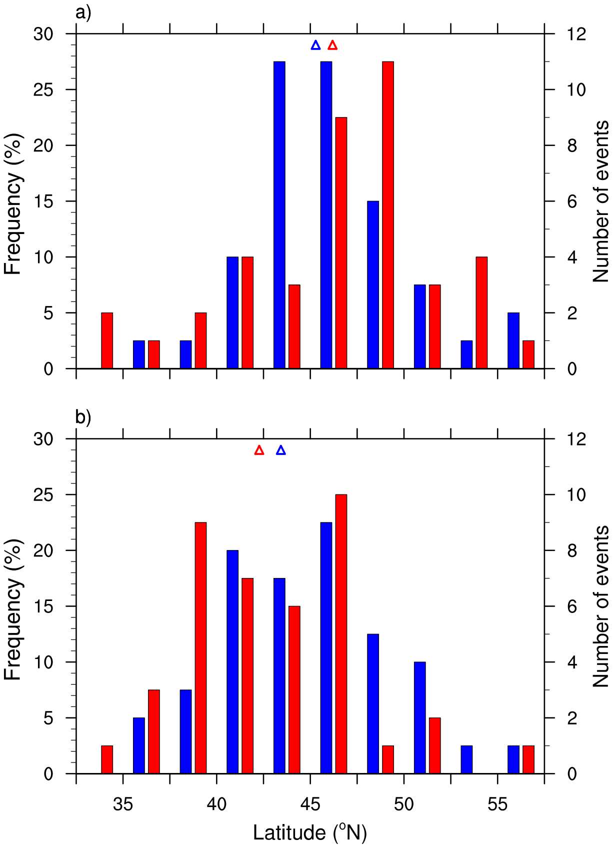

FIG. 4. Histograms of top 40 extreme events in HiRAM simulations on the (a) western and (b) eastern slopes as functions of latitude in the control (blue bars) and 2 × CO_2 (red bars) simulations. Blue and red triangles indicate the mean latitudes of extreme events in the control and 2 × CO_2 climates, respectively.

of top 10 events simulated with WRF on the 12-km fine mesh.

The western-slope extreme event is produced by a so-called atmospheric river, a narrow filament of concentrated moisture carried poleward from the subtropics (Zhu and Newell 1994). Recent studies based on observational data from western Europe and along the west coast of the United States show that atmospheric rivers are often responsible for heavy and extreme precipitation (Ralph et al. 2006; Warner et al. 2012; Lavers et al. 2012; Lavers and Villarini 2013). As is apparent in Fig. 6a, the axis of the atmospheric river is nearly perpendicular to the mountain, and it coincides with a jet of strong cross-mountain flow as evident from the strong gradient in the geopotential height field. Strong orographic lifting condenses large amounts of water vapor that precipitates out over the mountain. The contrast between the atmospheric river's WVP to east and west of the mountain clearly shows this drying.

TABLE 1. Thresholds of 24-h accumulated precipitation (mm) that select the (top) 40 and (bottom) 10 most extreme events in the HiRAM control simulation over the western and eastern slopes. Also listed are the number of events in the 2 × CO_2 simulation that exceed those threshold values.

	Western		Eastern	
	Control	2 × CO_2	Control	2 × CO_2
Threshold	105.1 mm		70.6 mm	
No. of events	40	128	40	116
Threshold	124.8 mm		86.4 mm	
No. of events	10	42	10	47

The eastern-slope extreme event in Fig. 6b is caused by a cutoff low to the southwest of the precipitation site, which produces strong southeasterlies over the eastern slope of the mountain. A plume of concentrated moisture is embedded in the southeasterly flow. A very high-amplitude ridge keeps the main jet stream well to the north of the cutoff low. Figure 7 shows a sounding from the location of the blue dot in Fig. 6b, upstream of the eastern slope. The atmosphere between 850 and 500 hPa is completely saturated and nearly moist neutral; the upslope easterly winds in this layer are roughly 18 m s^{-1} (35 knot).

While flow patterns like that shown in Fig. 6b are less common in the real world than western-slope atmospheric river events, close atmospheric analogs do occasionally occur. For example, the record-breaking rainfall across the Colorado Front Range between 11 and 13 September 2013 (Schwartz 2014) occurred in a synoptic setting resembling that in Fig. 6b. The basic structure of the geopotential height field for the Colorado event, shown in Fig. 8a, is similar to that in Fig. 6b, with a cutoff low south of a high-amplitude ridge. The 1200 UTC sounding from Denver, Colorado, on 12 September 2013 (Fig. 8b) also shows a similar deep layer of saturated, neutrally stratified flow, although the easterly winds in that layer are somewhat weaker than those in Fig. 7.

5. Changes in extreme-event intensity

Perhaps surprisingly, the mean sensitivity of the precipitation in the top 10 events to global warming is about 2% K^{-1} higher on the eastern side (where it is 5.9% K^{-1}) than on the west side (where it is 4.2% K^{-1}).[2] These values are comparable to the sensitivities for the vertically integrated condensation rate in the air columns

---

[2] Top 40 events from the HiRAM simulations show similar sensitivities: 6.3% K^{-1} over the eastern slopes and 3.9% K^{-1} to the west.

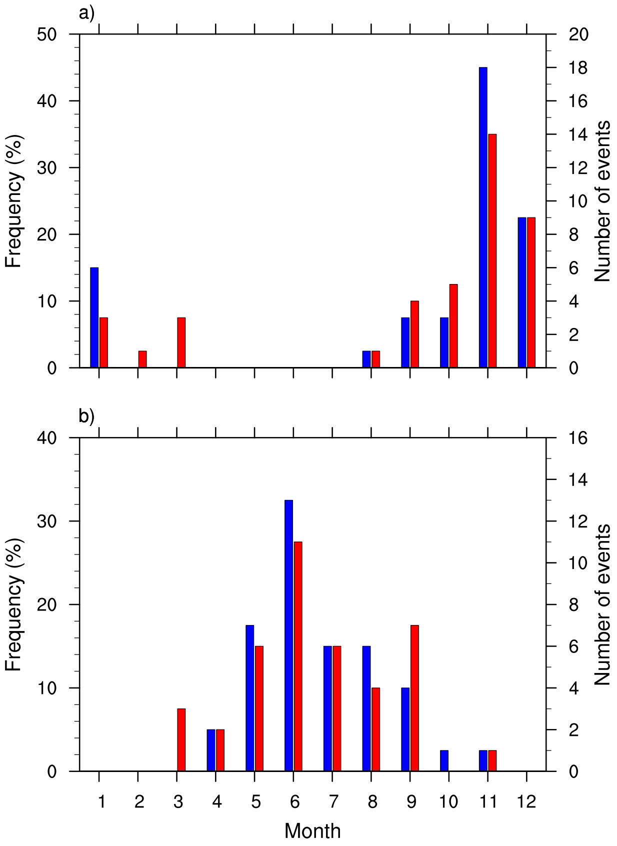

FIG. 5. Histograms of top 40 extreme events in HiRAM simulations on the (a) western and (b) eastern slopes as functions of calendar month in the control (blue bars) and 2 × CO_2 (red bars) simulations.

at the same time and location of each of the extreme events, which are 6.5% and 4.7% K^{-1} for the eastern and western sides, respectively.

The differences between the sensitivities in precipitation and condensation are due to changes in the precipitation efficiency, defined as the event-integrated precipitation divided by the event-integrated condensation. The precipitation efficiencies in these extreme events over our 120-km half-width mountains are relatively high, ranging from an average of 0.82 for the 10 western slope events in the doubled-CO_2 climate to 0.96 over the eastern slope in the control climate. These precipitation efficiencies are likely high because of the broad width of our mountains and the absence of embedded convection (Cannon et al. 2012). On both sides of the mountain, the precipitation efficiency decreases modestly as the planet warms, with the sensitivities of precipitation efficiency being −0.7% and −0.4% K^{-1} over the eastern and western sides, respectively. These sensitivities are qualitatively consistent with the findings in Kirshbaum and Smith (2008) that precipitation efficiency decreases with increases in the local temperature upstream of idealized horizontally uniform moist flow over a three-dimensional ridge.

a. Partitioning the sensitivities into thermodynamic and dynamic contributions

In our simulations, the sensitivity of the precipitation to changes in global mean temperature is dominated by the sensitivity of the event-integrated condensation. We therefore focus further analysis on those factors responsible for the changes in condensation, separating the effects of thermodynamic and dynamical changes in the condensation during those events. The local condensation rate c in the extreme precipitation events may be estimated by assuming moist adiabatic lifting maintains the water vapor content of the rising air at saturation, that is,

$$c = -w\frac{dq_s}{dz} = w\gamma_s\,, \tag{3}$$

where w is vertical velocity, q_s is saturation specific humidity, and $\gamma_s = -dq_s/dz$ is the lapse rate of saturation specific humidity.[3] Over 95% of the precipitation in the extreme orographic precipitation events in the 12-km WRF simulations is produced by grid-resolved physical processes; the remainder (less than 5%) is from parameterized convection. Thus (3) can be applied directly to the archived model data to approximate the condensation rate in each saturated grid cell. Integrating (3) vertically, one gets the total condensation in an air column,

$$C = \sum_k s_k c_k\,, \tag{4}$$

where the summation is limited to saturated grid cells by defining

$$s_k = \begin{cases} 0, & \text{if unsaturated,} \\ \Delta p_k/g, & \text{otherwise,} \end{cases} \tag{5}$$

here Δp_k is the pressure thickness of layer k and g is the gravitational constant. One can further average C over time and area for each extreme event (the 24 h and the 108 km × 108 km square on the mountain slope receiving most precipitation; denoted by an overbar), and then average results of the 10 events in either the control or the doubled-CO_2 climate (denoted by angle brackets) to obtain the mean condensation rate for the extremes:

---

[3] An analytic expression for γ_s as a function of temperature and pressure is provided in Shi and Durran (2014).

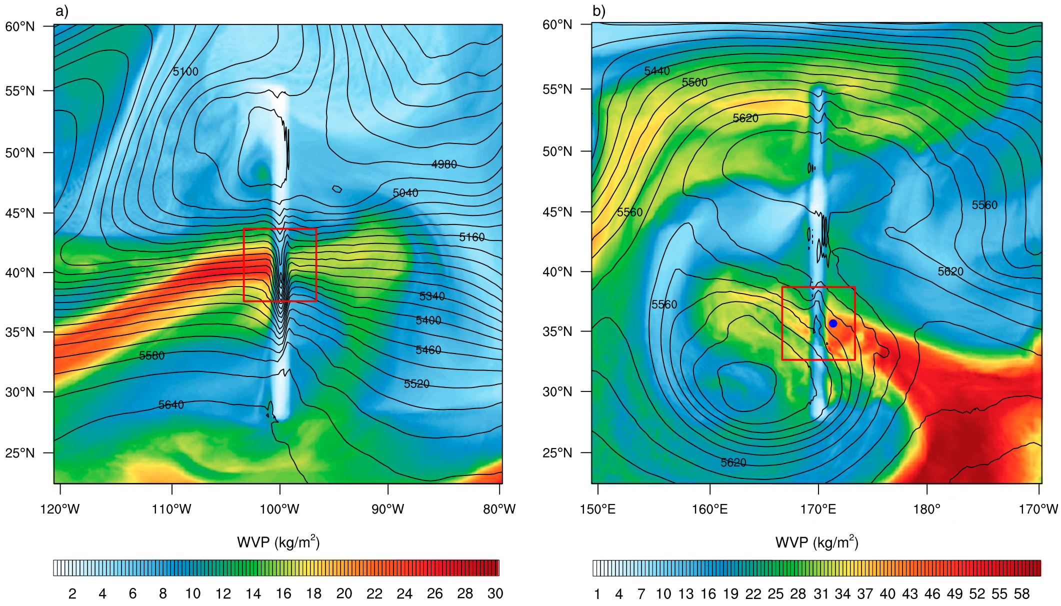

FIG. 6. Snapshots of WVP and 500-hPa geopotential height (black contours) in (a) one western-slope extreme event and (b) one eastern-slope extreme event. The interval between geopotential height contours is 30 m. Note that (a) is an event in the control climate and (b) is an event in the 2 × CO_2 world. Red boxes indicate the north–south extent of the mountainous region receiving intense rainfall. The mountain coincides with the north–south zone of reduced WVP in the center of each panel.

$$\langle \overline{C} \rangle = \left\langle \overline{\sum_k s_k c_k} \right\rangle . \tag{6}$$

Letting subscripts w and c denote the doubled-CO_2 and control climates, the change in mean condensation due to warming is

$$\delta \langle \overline{C} \rangle = \langle \overline{C} \rangle_w - \langle \overline{C} \rangle_c . \tag{7}$$

If one could pair the precipitating columns in a control climate event with the columns in a warmed climate event so that each pair of columns has the same saturated levels and the same time and space distribution, one could separate $\delta\langle\overline{C}\rangle$ into two contributions,

$$\left\langle \overline{\sum_k s_k[(c_k)_w - (c_k)_c]} \right\rangle = \left\langle \overline{\sum_k s_k \delta(w\gamma_s)_k} \right\rangle \approx \sum_k s_k[\overline{(w\delta\gamma_s)_k} + \overline{(\gamma_s \delta w)_k}], \tag{8}$$

where δ again denotes the change between warm and control climate values. In (8), the terms involving $w\delta\gamma_s$ and $\gamma_s\delta w$ would estimate the contributions from thermodynamical and dynamical changes, respectively. Such pairing, however, is not possible because the number of saturated layers is typically greater in the warmer climate.

Nevertheless, we can still estimate the two terms on the right side of (8) as follows. The thermodynamic contribution is evaluated as

$$\delta\langle\overline{C}\rangle_{\text{thrm}} = \frac{\sum_k \overline{(s_k w_k)}_w \delta\langle\overline{\gamma_s}\rangle_k + \sum_k \overline{(s_k w_k)}_c \delta\langle\overline{\gamma_s}\rangle_k}{2} . \tag{9}$$

During these extreme events, the lapse rate of saturation specific humidity varies with height but is almost uniform in the horizontal over each 108 km × 108 km square and 24-h period, so its change is well captured by $\delta\langle\overline{\gamma_s}\rangle_k$. The same is not true for the vertical velocity, which varies systematically in the cross-mountain direction and also exhibits substantial fluctuations in the along-slope direction. Within each 108-km north–south strip, the extreme precipitation is dominated by the cells with the strongest vertical velocities. Therefore, in estimating the dynamic contribution to (8), the simple time and space average used to obtain $\delta\langle\overline{\gamma_s}\rangle_k$ is replaced by $\delta\langle\tilde{w}_i\rangle_k$, where i indexes the cells in the cross-ridge direction and, for any given i, $\tilde{w}_i$ denotes the time average of the maximum w in the along-ridge direction. The dynamic contribution is then computed as

$$\delta\langle\overline{C}\rangle_{\text{dyn}} = \frac{\sum_{i,k} \overline{(s_{i,k}\gamma_{s_{i,k}})}^{y,t}_w \delta\langle\tilde{w}_i\rangle_k + \sum_{i,k} \overline{(s_{i,k}\gamma_{s_{i,k}})}^{y,t}_c \delta\langle\tilde{w}_i\rangle_k}{2N_i}, \tag{10}$$

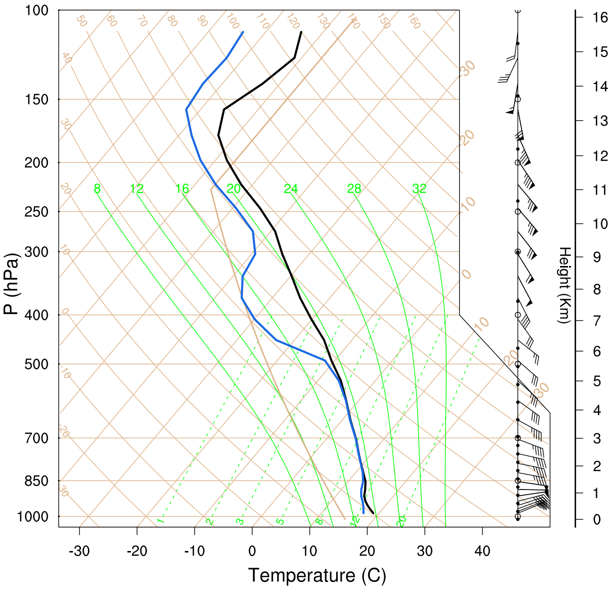

FIG. 7. The sounding and winds in an extreme event plotted on a skew T–log$p$ chart. The sounding is taken at the same simulation time at the location upstream of the mountain indicated by the blue dot within the red box in Fig. 6b. The black curve is temperature and the blue curve is dewpoint.

where $N_i = 9$ is the number of cells in the east–west direction included in the event average, and the y, t notation to the right of the overbar denotes event averages taken in the 108-km north–south direction and over the 24-h time period.

Over the eastern slopes, $\delta\langle\overline{C}\rangle_{\mathrm{thrm}}/\langle\overline{C}\rangle_c = 3.9\%\ \mathrm{K}^{-1}$, $\delta\langle\overline{C}\rangle_{\mathrm{dyn}}/\langle\overline{C}\rangle_c = 3.2\%\ \mathrm{K}^{-1}$, and their sum provides a good approximation to the true value of $\delta\langle\overline{C}\rangle/\langle\overline{C}\rangle_c = 6.5\%\ \mathrm{K}^{-1}$ (exceeding it by 9%). Over the western slope the same thermodynamic and dynamic sensitivities are 5.0% and $0.03\%\ \mathrm{K}^{-1}$, whose sum differs from the total sensitivity $4.7\%\ \mathrm{K}^{-1}$ by just 6%. The thermodynamic sensitivity is somewhat stronger over the western slopes of the mountains than over the eastern slopes, which might be expected because most western-slope extreme events occur during winter whereas the eastern-slope extremes are mostly summertime phenomena, and $\partial(\ln\gamma_s)/\partial T$ is larger at colder temperatures (Shi and Durran 2014; Siler and Roe 2014).

By far the largest east–west contrast in sensitivities is in the dynamical contribution. The large eastern-slope dynamic sensitivity more than compensates for its weaker thermodynamic sensitivity and is responsible for the eastern side having a much larger value of $\delta\langle\overline{C}\rangle/\langle\overline{C}\rangle_c$ than the western side. A closer look at this dynamical enhancement is provided in the next section.

b. *Source of the dynamical enhancement*

The dynamical contribution to the changes in extreme events arises from the differences between $\tilde{w}_i$ in the control and warmer climates. These differences are illustrated by the vertical profiles of $\tilde{w}_i$ in Fig. 9 for three different cross-ridge locations above the eastern and the western slopes. Consistent with the negligible value of $\delta\langle\overline{C}\rangle_{\mathrm{dyn}}/\langle\overline{C}\rangle$ over the western slopes, Figs. 9a–c show

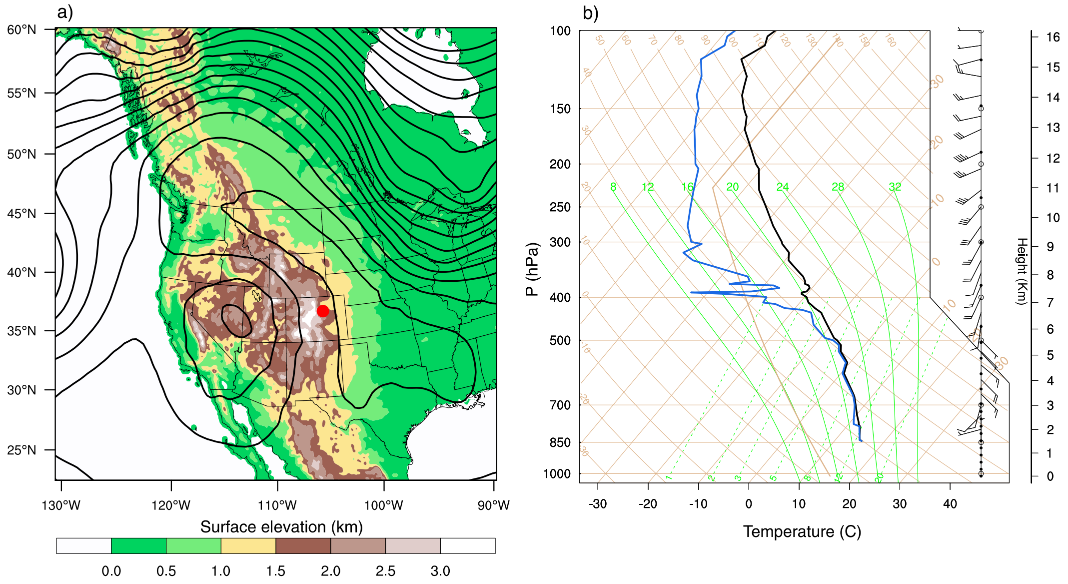

FIG. 8. (a) The 500-hPa level geopotential (height contoured at 30-m intervals) for 1200 UTC 12 Sep 2013 and (b) the sounding from Denver, Colorado, at the same time. Red dot in (a) indicates the geographic location of Denver. Data in (a) are from the National Centers for Environmental Prediction (NCEP) final operational global analysis (FNL).

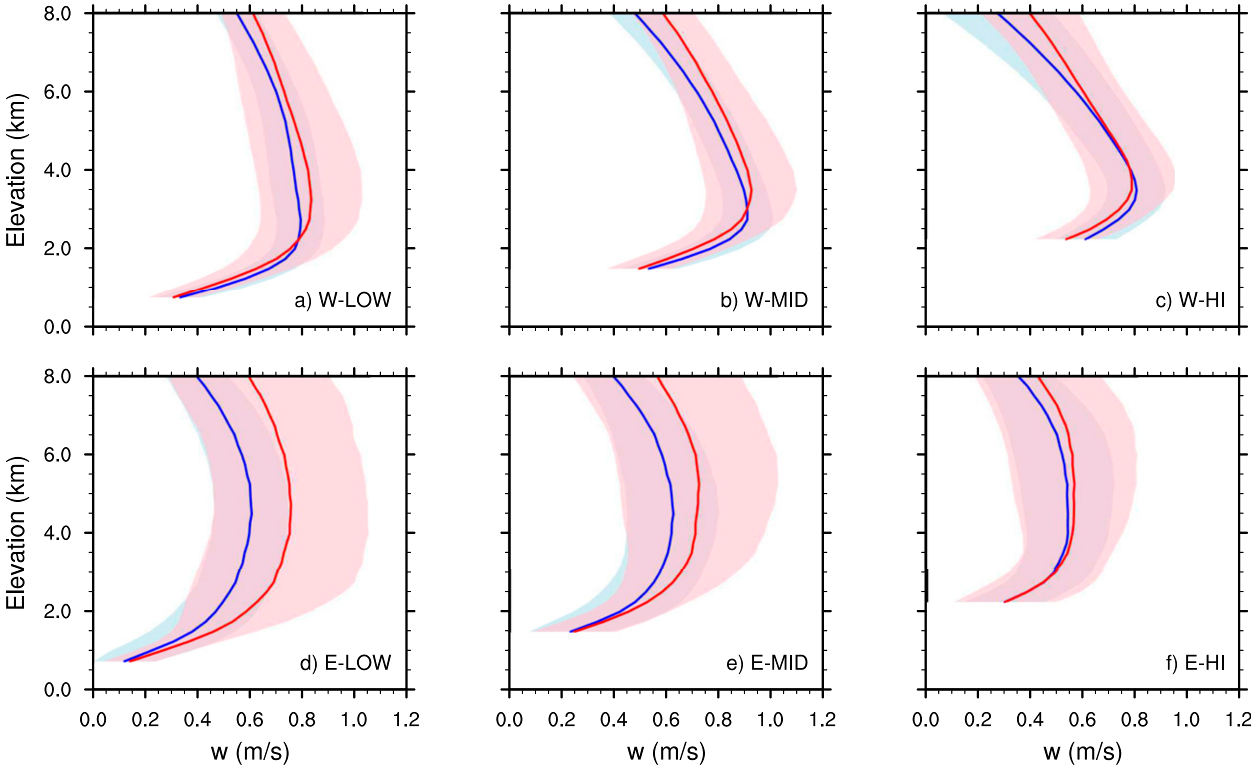

FIG. 9. Profiles of mean $\tilde{w}_i$ over the (a)–(c) western and (d)–(f) eastern slopes, for (left) low (0.75 km), (center) middle (1.5 km), and (right) high (2.25 km) surface elevations of the mountains. Blue curves are profiles in the control climate, and red curves are profiles in the $2 \times CO_2$ climate. Event scatter in the control and $2 \times CO_2$ climates is shown by light blue and light pink shading, using one standard deviation of $\tilde{w}_i$ in each 10-event set.

almost no change in the vertical velocity profiles between the control and the warmer climates. In contrast, on the eastern side, $\tilde{w}_i$ increases significantly as the climate warms at the lower and midslope elevations (Figs. 9d,e).

The vertical motions in extreme precipitation events over mountains are governed by mountain wave dynamics, as illustrated by the vertical velocity cross sections passing through the updraft cores for four representative events plotted in Fig. 10. In these moist events, the effective stability in the middle and lower troposphere is weak, so the vertical wavelength of the waves is long and the axes of their updrafts and downdrafts extend almost straight upward to a height around 7 km. The upstream tilt with height of the phase lines in these waves is more pronounced in the stratosphere and upper troposphere. As indicated by the green contours, most of the condensation responsible for the precipitation extremes occurs at low levels in the updrafts above windward slopes.

The depth and intensity of this windward ascent depends on the propagation and reflection of mountain waves. In particular, Siler and Durran (2015), using linear theory and numerical simulations, showed that the partial reflection of mountain waves at the tropopause can have an important impact on the vertical motions over mountains and the resulting precipitation. Here we compare the lower-tropospheric vertical velocities forced by the mean background atmospheric structures during the extreme events in the control and warmer climates. We compute these velocities using the linear hydrostatic mountain wave model of Klemp and Lilly (1975), which assumes the atmosphere is incompressible and consists of three layers with constant static stabilities N and constant wind shear in each layer.

For the eastern-slope means, we neglect the vertical variations of the winds with height, which is a reasonable approximation to the actual average upstream flow. Those relatively uniform easterly winds extend up through troposphere until finally encountering a critical level (where the cross-mountain easterlies drop to zero) in the lower stratosphere.[4] In the context of the linear model, wave absorption at the critical level is represented by an upper boundary condition requiring that all wave energy propagation be upward.

---

[4] As an example, see the winds for one specific event in Fig. 7.

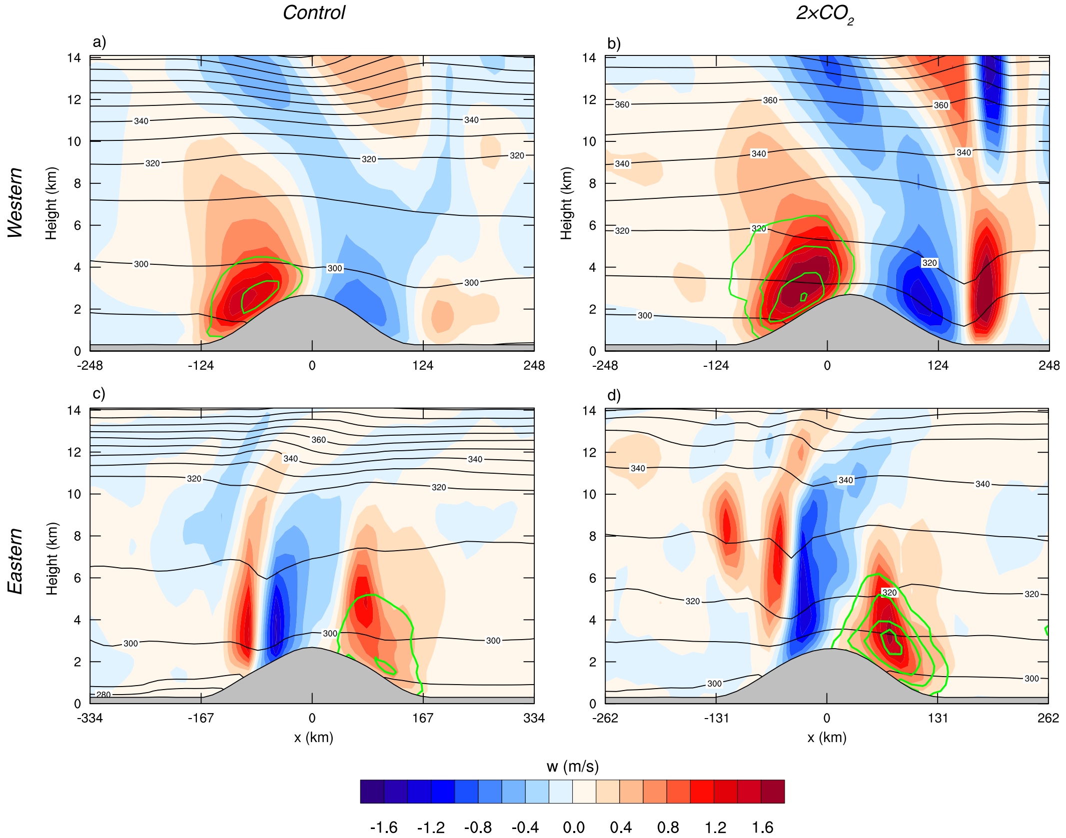

FIG. 10. Snapshots of vertical velocity (color shading) and potential temperature (black contours; K) field on cross sections through the centers of precipitation maxima over the (top) western slopes and (bottom) eastern slopes for (a),(c) extreme events in the control climate and (b),(d) the 2 × CO$_2$ climate. Also shown in green are contours of the condensation rate at contours of 2, 4, 6, and 8 g kg^{-1} h^{-1}. These cross sections are taken parallel to the mean wind direction in the lower troposphere. For (a),(b), the winds are nearly from due west; for (c),(d), the winds are from the southwest.

Assuming a vertically uniform mean cross-mountain wind U, the steady-state two-dimensional solution in the lowest layer for a single Fourier component $w_L = \Re\{\hat{w}_1(z)e^{ikx}\}$ is

$$\hat{w}_1 = ikUh_m\left[\cos\left(\frac{N_1}{U}z\right) + \alpha\sin\left(\frac{N_1}{U}z\right)\right], \qquad (11)$$

where

$$\alpha = \frac{N_1\sin\phi_1 + N_2\beta\cos\phi_1}{N_1\cos\phi_1 - N_2\beta\sin\phi_1},$$

$$\beta = \frac{N_2\sin\phi_2 + iN_3\cos\phi_2}{N_2\cos\phi_2 - iN_3\sin\phi_2},$$

and

$$\phi_j = \frac{N_j}{U}(z_j - z_{j-1}) \quad \text{for} \quad j = 1, 2.$$

The subscripts in the above expressions denote the respective layers; h_m is the mountain height (2.5 km), z_j is the elevation of the top of layer j, and $z_0 = 0$. We shall consider only the solution for a single wavenumber k that matches the mountain width ($2a = 240$ km) in our WRF simulations, although the solution for a particular mountain shape can be readily constructed using Fourier transforms.

During extreme precipitation events the atmosphere has a three-layer structure formed by a saturated and moist nearly neutral lower troposphere, topped by the dry upper troposphere and the stratosphere, with the stratosphere having the largest stability. The air in the lowest layer may become unsaturated on the lee side of mountains because of descent, but previous studies suggest that despite the presence of such unsaturated regions, the effective bulk static stability of the lowest layer N_1 is very close to the moist Brunt–Väisälä frequency (Jiang 2003; Siler and Durran 2015). In addition, we found that for our specific application, there was little sensitivity to doubling or halving N_1.

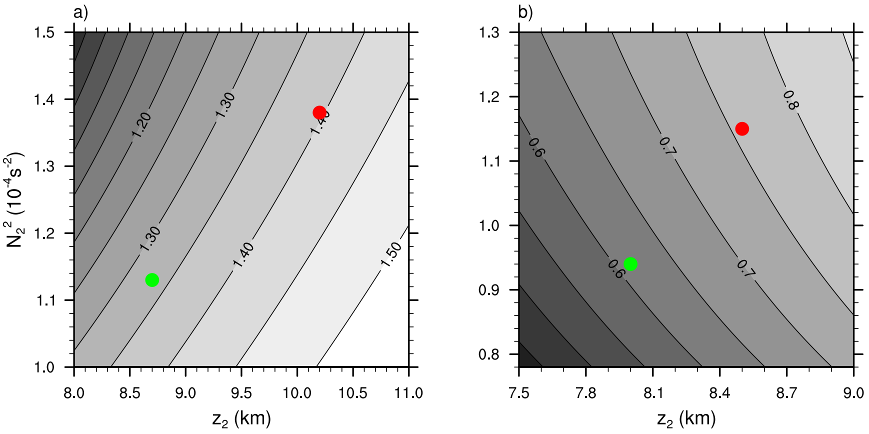

FIG. 11. Vertical velocities w_L in linear mountain waves at height 1.5 km above the middle point of the (a) western and (b) eastern slope as a function of tropopause height z_2 and the static stability of upper troposphere N_2. Green and red dots indicate the extreme-event mean values in the control and doubled-CO$_2$ simulations, respectively. Contour interval is 0.05 m s^{-1}.

Following Durran (1992), who suggested that the linear tropopause tuning criteria of Klemp and Lilly (1975) works best when adjusted for finite-amplitude mountains by setting z_2 equal to the actual tropopause height minus $3h_m/2$, in the control and warmer climates, z_2 is specified as 8.0 and 8.5 km, respectively. The mean upper tropospheric moist static stability gives N_2^2 as 0.94×10^{-4} and 1.15×10^{-4} s^{-2} in the control and warmer climates. Increases in midlatitude static stability are a robust response to global warming in climate simulations (Frierson 2006), and the rise in tropopause height resulting from CO$_2$ increases has been seen in both observations and climate model simulations (Kushner et al. 2001; Santer et al. 2003). The depth of the saturated layer is well approximated as $z_1 = z_2 - 5$. The other parameters required to evaluate (11) remain almost the same in the control and warmer climates; we estimate these values as $N_1^2 = 2.5 \times 10^{-5}$ s^{-2}, $N_3^2 = 4.0 \times 10^{-4}$ s^{-2}, and $U = 15$ m s^{-1}.

Although the warming-induced increase in z_1 is comparable to that for z_2, the windward ascent in the three-layer model turns out to be insensitive to that change over the parameter regime of interest. Figure 11 shows the dependence of w_L at 1.5 km above the center of the windward slope (near the region of maximum orographic condensation) on the other two key parameters, z_2 and N_2. The extreme-event mean values for the control and the warmer climate are indicated by the green and red dots, respectively. Despite its limited dynamics, the linear model provides a good estimate of the mean vertical velocity over the eastern slope (cf. Figs. 9e and 11b). Moreover, the 2.3% K^{-1} sensitivity of $\delta w_L/w_L$ reasonably approximates the 2.8% K^{-1} sensitivity of then extreme-event-averaged vertical velocity $\delta\tilde{w}/\tilde{w}$ at the same 1.5-km level above the center of the windward slope.

Therefore, the enhanced vertical motion in eastern-slope extreme events occurs because the atmosphere has become better tuned to produce strong mountain waves. One may ask why the western-slope extreme events do not have significant dynamical enhancement. The answer is that the background wind speeds during western-slope events make it much more difficult to produce a similar degree of mountain wave enhancement. The changes in tropopause height and upper tropospheric static stability for the western-slope events are actually somewhat larger than those for the eastern-slope cases. As the climate warms, z_2 increases from 8.7 to 10.2 km, and N_2 increases from 1.13×10^{-4} to 1.38×10^{-4} s^{-2}. The sensitivity of w_L to these changes is, nevertheless, much reduced because the cross-mountain winds are much stronger during the western-slope events. The average extreme-event winds are a roughly uniform 15 m s^{-1} in the east, whereas they range from about 20 m s^{-1} at the top of boundary layer to 60 m s^{-1} near the tropopause in the west. Figure 11a shows how this change in the upstream winds modifies the changes in w_L. The computation in Fig. 11a uses the full Klemp and Lilly (1975) linear model including shear such that the winds vary linearly from 20 to 60 m s^{-1} between the ground and the tropopause. The vertical velocities in Fig. 11a are roughly 50% larger than the average values for a point 1.5 km above the surface in Fig. 9b, presumably due to the simplified dynamics in the linear model (neglect of finite-amplitude and three-dimensional effects, no boundary layer or moisture). Nevertheless, they both exhibit almost negligible sensitivities to warming ($\delta w_L/w_L = 0.01\%$ K^{-1} and $\delta\tilde{w}/\tilde{w} = -0.05\%$ K^{-1}).

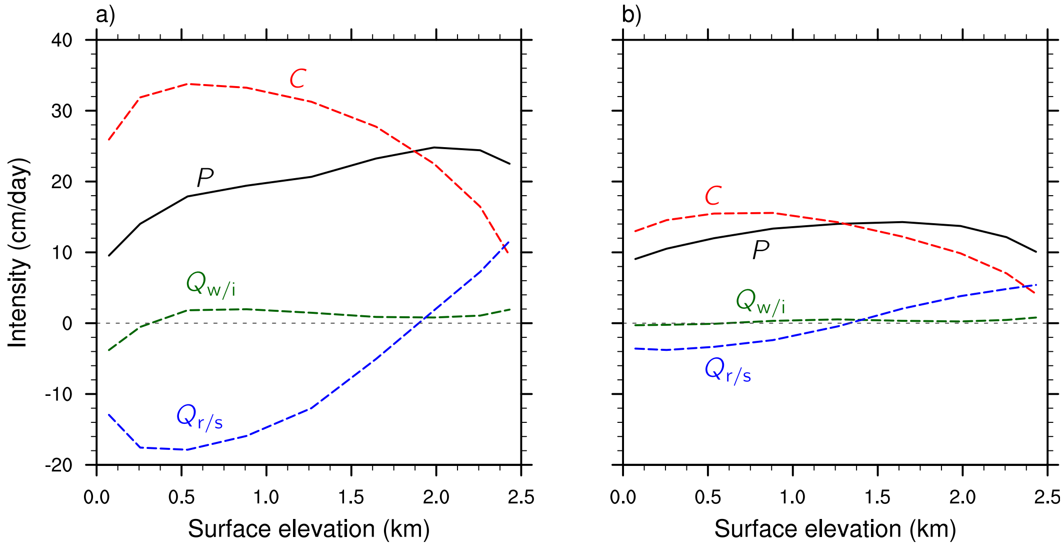

FIG. 12. The 24-h mean intensity of surface precipitation (P), column integrated condensation (C), and column integrated convergence of rain and snow ($Q_{r/s}$) and of cloud water and ice ($Q_{w/i}$) in the control climate (a) western-slope and (b) eastern-slope extreme events. Negative values indicate divergence.

6. Elevational dependence

Extreme orographic precipitation and its sensitivity to global warming both vary with elevation. The fraction of precipitation that falls as snow and its vertical distribution can have a major impact on runoff and flooding (Hamlet and Lettenmaier 2007). For example, hydrological model forecasts for several California watersheds suggest that a 660-m increase in the elevation of the melting level can triple the runoff during 24-h rainfall events (White et al. 2002).

As shown by the black curves in Fig. 12, the 24-h extreme-event-averaged precipitation rate P in the control climate increases with elevation until about $0.8h_m$ (a height of 2 km), and the elevation dependence is more pronounced over the western slopes than in the east. Also plotted in Fig. 12 are the column-integrated individual terms in the surface precipitation budget: the condensation rate C, the horizontal flux convergence of rain and snow $Q_{r/s}$, and the convergence of cloud water and cloud ice $Q_{w/i}$. When integrated over a 24-h period, the sources and sinks of the hydrometeors in a column extending from Earth's surface to the top of the atmosphere should balance such that

$$P = C + Q_{w/i} + Q_{r/s}. \qquad (12)$$

In contrast to the precipitation, as shown in Fig. 12, the column integrated condensation is maximized over the lower part of the mountain and decreases as the surface elevation rises. The difference between P and C is almost completely accounted for by $Q_{r/s}$ because of the variations in the downwind transport of rain drops and snow. The magnitude and variation in $Q_{r/s}$ is greater over the western slopes than in the east because, in the west, more extreme precipitation events occur in wintertime when the upslope westerlies are stronger and there are more slowly falling snow particles available for advection. In contrast to C and $Q_{r/s}$, $Q_{w/i}$ makes only a small contribution to the precipitation budget.

Neglecting the small contribution from $Q_{w/i}$ [(12)], the sensitivity of the mean column-integrated precipitation rate to increased CO_2 satisfies

$$\frac{\delta P}{P} = \frac{\delta C}{P} + \frac{\delta Q_{r/s}}{P}. \qquad (13)$$

The amplitude of each term in (13) is shown in Fig. 13. While the sensitivity of condensation ($\delta C/C$) shows little dependence on surface elevation (not shown), the sensitivity of precipitation ($\delta P/P$) and the contribution of condensation ($\delta C/P$) generally decrease with elevation. This is primarily because the factor $1/P$ decreases with elevation (Fig. 12). For the eastern-slope events, the normalized changes in condensation ($\delta C/P$ account for most of the precipitation sensitivity, but over the upper part the western slope events (between elevations of 1.4 and 2.2 km) $\delta P/P$ is much smaller than $\delta C/P$. This difference between $\delta P/P$ and $\delta C/P$ is associated with large negative values of $\delta Q_{r/s}/P$ over the same upper part of the western slope. These negative values of $\delta Q_{r/s}/P$ arise almost entirely because the column-integrated horizontal flux of snow becomes more divergent above the upper slopes of the mountain in the warmer climate.

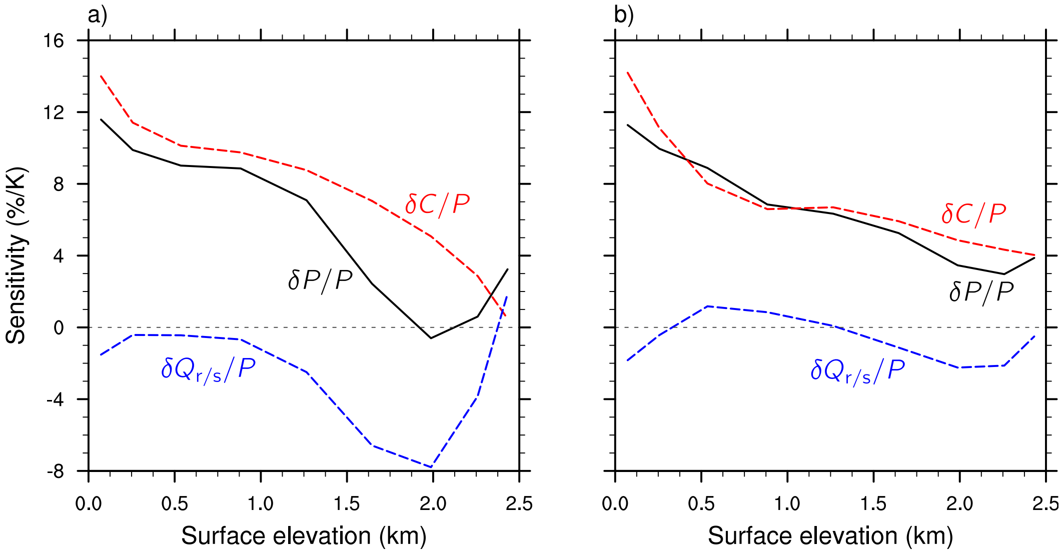

FIG. 13. Contributions of the changes in the column-integrated condensation ($\delta C/P$) and the column-integrated rain–snow convergence ($\delta Q_{r/s}/P$) to the elevational dependence of the sensitivity of precipitation extremes ($\delta P/P$) in (a) western-slope and (b) eastern-slope events.

Separating the detailed factors responsible for the increased divergence of $Q_{r/s}$ in the warmer climate is rather involved, but the common denominator is the rise in the melting level. In those extreme events, the melting level in the warmer climate rises by about 1 km in our simulations via processes detailed in Minder et al. (2011). As a consequence, most of the surface precipitation above a height of 500 m switches from snow to rain (Fig. 14), which as noted previously could produce more runoff and flooding during these extreme events.

7. Summary and discussion

The processes responsible for changes in midlatitude extreme orographic precipitation in a warmer world have been examined using a hierarchy of models to effectively simulate 40 years of weather over an idealized north–south ridge on the western margin of a continent very roughly representative of western North America. Control and doubled-CO_2 climates were computed using the GFDL HiRAM, and the top ten 24-h precipitation events on the western and eastern mountain slopes in both climates were resimulated at higher resolution with WRF.

The extreme precipitation events on the western and eastern slopes of the idealized mountains tend to occur in different seasons and under different weather patterns. The western-slope events mostly occur in winter months, when a strong atmospheric river embedded in a westerly jet impinges on the western side of the mountains. The eastern-slope events occur most frequently in summertime, when a cyclone to the south produces southeasterly winds and an intense plume of moisture impinges on the slopes of the region experiencing heavy rainfall. Several of the eastern-slope extreme events

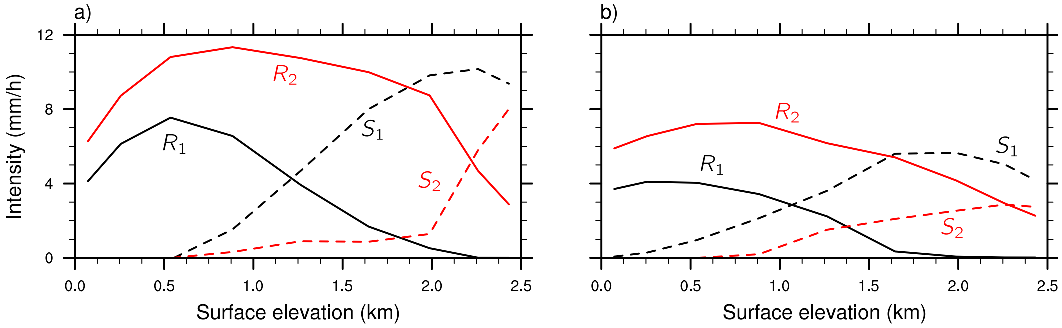

FIG. 14. The 24-h mean intensity of surface rain (R) and snow (S) of (a) western-slope and (b) eastern-slope extreme events in the control (black) and warmed (red) climate. The subscripts 1 and 2 indicate values for the 1 × CO_2 and 2 × CO_2 climates, respectively.

exhibited synoptic weather patterns strikingly similar to the 11–13 September 2013 floods along the Colorado Front Range.

The 24-h precipitation intensities for the top-10-event WRF simulations increased on the eastern side by 5.9% K^{-1} of global-averaged surface temperature increase, and by a somewhat smaller 4.2% K^{-1} on the western side. Similar values of 6.3% K^{-1} over the eastern slopes and 3.9% K^{-1} in the west were obtained for the top 40 events in the HiRAM simulations. The vertically integrated condensation rate for the top-10-event WRF simulations gave a good approximation to the sensitivity of the precipitation to global warming, including the roughly 2% K^{-1} difference in the sensitivity between the eastern and western slopes.

The thermodynamic sensitivity of condensation in eastern-slope and western-slope precipitation extremes is estimated as 3.9% and 5.0% K^{-1}, respectively. These values are close to previous estimates by Shi and Durran (2014) for general orographic precipitation on the windward side of midlatitude mountains under the assumption that the incoming flow is saturated (as in these extreme events). Under these conditions, the thermodynamic sensitivity ranged between 4% and 5% K^{-1} ($\delta\Gamma_s/M$ in their Fig. 11). The thermodynamic sensitivity for the western-slope extreme events here is about 1% K^{-1} greater than that for the warmer summertime events over the eastern slope. This is consistent with their wintertime occurrence at colder temperatures.

The difference between the thermodynamic sensitivity of eastern and western slope extremes was overshadowed by a 3% K^{-1} greater dynamical contribution to precipitation sensitivity in the east than in the west because of differences in the vertical velocity. The sensitivity of the vertical velocities driving the eastern- and western-slope events was well approximated by a three-layer linear mountain wave model and is due to warming-induced increases in upper tropospheric static stability and the tropopause height. The difference in sensitivity for the eastern- and western-slope vertical velocities is primarily due to differences in the strength of the mean cross-mountain flow, with much weaker winds occurring during the eastern-slope events. Higher precipitation sensitivities might have been expected to occur on the eastern side through an alternate thermodynamic mechanism proposed by Siler and Roe (2014). They noted that under moist saturated conditions, increases in surface temperature produce relatively more condensation aloft, which is more easily advected downwind of the crest to fall on the lee slope. None of the extreme eastern-slope events in our simulations involves significant westerly flow at the mountain crest, and as a consequence their downwind advection mechanism is not active.

Although the precipitation thresholds defining our extreme events shift with the climate to remain “once per year” and “once per four year” events, the number of events exceeding the control climate thresholds increases dramatically in the warmer world. On both sides of the mountain, once-per-year events in the control climate occur on average three times per year in the warmer world. Once-per-four-year events shift, on average, to once every year.

The sensitivity of the precipitation to warming generally decreases with altitude in the WRF simulations, although much of this change is simply due to the way the baseline control climate precipitation increases with elevation. An exception occurs over the western slopes on the upper portion of the mountain, where the precipitation sensitivity is further reduced by an increase in the column-averaged divergence of snow and rain. This increased divergence is related to an increase in the height of the melting level in the warmer climate. The most important impact of the change in melting level, however, is to produce a major shift from snow to rain over much of the mountain slope. Such shifts during extreme events have the potential to produce much more runoff and flooding over mountain slopes.

Clearly one must expect quantitative differences between these idealized simulations and climate-model simulations of extreme precipitation over any actual midlatitude mountain range, and further study is required to determine specific real world responses. Nevertheless, the general physical basis for the changes in midlatitude orographic precipitation extremes revealed by our idealized simulations may have widespread applicability. One piece of evidence supporting this comes from Diffenbaugh et al. (2005) and Singh et al. (2013), who, consistent with our result that eastern-slope extreme precipitation increases more rapidly than in the west, found a weakening of the orographic rain shadow in the warmer climate over the northwestern United States that was largely due to changes in extreme precipitation.

Acknowledgments. The authors have benefited from conversations with Dargan Frierson, David Battisti, and the comments of three anonymous reviewers. This research was supported by National Science Foundation (NSF) Grant AGS-1138977 and used the Extreme Science and Engineering Discovery Environment (XSEDE), which is supported by NSF Grant ACI-1053575.

APPENDIX

WRF Physics Schemes

Table A1 lists the WRF physics schemes used in simulations. Detailed descriptions of those schemes are

TABLE A1. List of WRF physics schemes.

Physical parameterization	Physics scheme
Microphysics	WRF single-moment 5-class microphysics scheme (WSM5)
Longwave radiation	Community Atmosphere Model (CAM)
Shortwave radiation	CAM
Surface layer	Fifth-generation Pennsylvania State University–NCAR Mesoscale Model (MM5)
Land surface	Noah
Planetary boundary layer	Yonsei University (YSU)
Cumulus parameterization	Kain–Fritsch

provided in Skamarock et al. (2008). Note that Singh and O'Gorman (2014) found the choice of microphysics scheme can affect the changes in precipitation extremes with warming.

REFERENCES

Beniston, M., 2005: Mountain climates and climatic change: An overview of processes focusing on the European Alps. *Pure Appl. Geophys.,* **162,** 1587–1606, doi:10.1007/s00024-005-2684-9.

Cannon, D. J., D. J. Kirshbaum, and S. L. Gray, 2012: Under what conditions does embedded convection enhance orographic precipitation? *Quart. J. Roy. Meteor. Soc.,* **138,** 391–406, doi:10.1002/qj.926.

Diffenbaugh, N. S., J. S. Pal, R. J. Trapp, and F. Giorgi, 2005: Fine-scale processes regulate the response of extreme events to global climate change. *Proc. Natl. Acad. Sci. USA,* **102,** 15 774–15 778, doi:10.1073/pnas.0506042102.

Durran, D. R., 1992: Two-layer solutions to Long's equation for vertically propagating mountain waves: How good is linear theory? *Quart. J. Roy. Meteor. Soc.,* **118,** 415–433, doi:10.1002/qj.49711850502.

Emori, S., and S. Brown, 2005: Dynamic and thermodynamic changes in mean and extreme precipitation under changed climate. *Geophys. Res. Lett.,* **32,** L17706, doi:10.1029/2005GL023272.

Frierson, F. M. W., 2006: Robust increases in midlatitude static stability in simulations of global warming. *Geophys. Res. Lett.,* **33,** L24816, doi:10.1029/2006GL027504.

Hamlet, A. F., and D. P. Lettenmaier, 2007: Effects of 20th century warming and climate variability on flood risk in the western U.S. *Water Resour. Res.,* **43,** W06427, doi:10.1029/2006WR005099.

Jiang, Q., 2003: Moist dynamics and orographic precipitation. *Tellus,* **55A,** 301–316, doi:10.1034/j.1600-0870.2003.00025.x.

Kharin, V. V., F. W. Zwiers, X. Zhang, and G. C. Hegerl, 2007: Changes in temperature and precipitation extremes in the IPCC ensemble of global coupled model simulations. *J. Climate,* **20,** 1419–1444, doi:10.1175/JCLI4066.1.

Kirshbaum, D. J., and R. B. Smith, 2008: Temperature and moist-stability effects on midlatitude orographic precipitation. *Quart. J. Roy. Meteor. Soc.,* **134,** 1183–1199, doi:10.1002/qj.274.

Klemp, J. B., and D. R. Lilly, 1975: The dynamics of wave-induced downslope winds. *J. Atmos. Sci.,* **32,** 320–339, doi:10.1175/1520-0469(1975)032<0320:TDOWID>2.0.CO;2.

Kushner, P. J., I. M. Held, and T. L. Delworth, 2001: Southern Hemisphere atmospheric circulation response to global warming. *J. Climate,* **14,** 2238–2249, doi:10.1175/1520-0442(2001)014<0001:SHACRT>2.0.CO;2.

Lavers, D. A., and G. Villarini, 2013: The nexus between atmospheric rivers and extreme precipitation across Europe. *Geophys. Res. Lett.,* **40,** 3259–3264, doi:10.1002/grl.50636.

——, ——, R. P. Allan, E. F. Wood, and A. J. Wade, 2012: The detection of atmospheric rivers in atmospheric reanalyses and their links to British winter floods and the large-scale climatic circulation. *J. Geophys. Res.,* **117,** D20106, doi:10.1029/2012JD018027.

Lin, Y.-L., S. Chiao, T.-A. Wang, M. L. Kaplan, and R. P. Weglarz, 2001: Some common ingredients for heavy orographic rainfall. *Wea. Forecasting,* **16,** 633–660, doi:10.1175/1520-0434(2001)016<0633:SCIFHO>2.0.CO;2.

Maddox, R., L. Hoxit, C. Chappell, and F. Caracena, 1978: Comparison of meteorological aspects of the Big Thompson and Rapid City flash floods. *Mon. Wea. Rev.,* **106,** 375–389, doi:10.1175/1520-0493(1978)106<0375:COMAOT>2.0.CO;2.

Marsaglia, G., W. W. Tsang, and J. Wang, 2003: Evaluating Kolmogorov's distribution. *J. Stat. Softw.,* **8** (18), 1–4.

Miller, L. H., 1956: Table of percentage points of Kolmogorov statistics. *J. Amer. Stat. Assoc.,* **51,** 111–121, doi:10.1080/01621459.1956.10501314.

Minder, J. R., D. R. Durran, and G. H. Roe, 2011: Mesoscale controls on the mountainside snow line. *J. Atmos. Sci.,* **68,** 2107–2127, doi:10.1175/JAS-D-10-05006.1.

O'Gorman, P. A., 2012: Sensitivity of tropical precipitation extremes to climate change. *Nat. Geosci.,* **5,** 697–700, doi:10.1038/ngeo1568.

——, and T. Schneider, 2009a: The physical basis for increases in precipitation extremes in simulations of 21st-century climate change. *Proc. Natl. Acad. Sci. USA,* **106,** 14 773–14 777, doi:10.1073/pnas.0907610106.

——, and ——, 2009b: Scaling of precipitation extremes over a wide range of climates simulated with an idealized GCM. *J. Climate,* **22,** 5676–5685, doi:10.1175/2009JCLI2701.1.

Ralph, F. M., P. J. Neiman, G. A. Wick, S. I. Gutman, M. D. Dettinger, D. R. Cayan, and A. B. White, 2006: Flooding on California's Russian River: Role of atmospheric rivers. *Geophys. Res. Lett.,* **33,** L13801, doi:10.1029/2006GL026689.

Rasmussen, K. L., and R. A. Houze, 2012: A flash-flooding storm at the steep edge of high terrain. *Bull. Amer. Meteor. Soc.,* **93,** 1713–1724, doi:10.1175/BAMS-D-11-00236.1.

Santer, B. D., and Coauthors, 2003: Contributions of anthropogenic and natural forcing to recent tropopause height changes. *Science,* **301,** 479–483, doi:10.1126/science.1084123.

Schwartz, C. S., 2014: Reproducing the September 2013 record-breaking rainfall over the Colorado Front Range with high-resolution WRF forecasts. *Wea. Forecasting,* **29,** 393–402, doi:10.1175/WAF-D-13-00136.1.

Shi, X., and D. R. Durran, 2014: The response of orographic precipitation over idealized midlatitude mountains due to global increases in CO_2. *J. Climate,* **27,** 3938–3956, doi:10.1175/JCLI-D-13-00460.1.

Siler, N., and G. Roe, 2014: How will orographic precipitation respond to surface warming? An idealized thermodynamic perspective. *Geophys. Res. Lett.,* **41,** 2606–2613, doi:10.1002/2013GL059095.

——, and D. Durran, 2015: Assessing the impact of the tropopause on mountain waves and orographic precipitation using linear theory and numerical simulations. *J. Atmos. Sci.,* **72,** 803–820, doi:10.1175/JAS-D-14-0200.1.

Singh, D., M. Tsiang, B. Rajaratnam, and N. S. Diffenbaugh, 2013: Precipitation extremes over the continental United States in a transient, high-resolution, ensemble climate model experiment. *J. Geophys. Res. Atmos.,* **118,** 7063–7086, doi:10.1002/jgrd.50543.

Singh, M. S., and P. A. O'Gorman, 2014: Influence of microphysics on the scaling of precipitation extremes with temperature. *Geophys. Res. Lett.,* **41,** 6037–6044, doi:10.1002/2014GL061222.

Skamarock, W. C., and Coauthors, 2008: A description of the Advanced Research WRF version 3. NCAR Tech. Note NCAR/TN-475+STR, 113 pp.

Warner, M. D., C. F. Mass, and E. P. Salathé Jr., 2012: Wintertime extreme precipitation events along the Pacific Northwest coast: Climatology and synoptic evolution. *Mon. Wea. Rev.,* **140,** 2021–2043, doi:10.1175/MWR-D-11-00197.1.

Wehner, M. F., 2013: Very extreme seasonal precipitation in the NARCCAP ensemble: Model performance and projections. *Climate Dyn.,* **40,** 59–80, doi:10.1007/s00382-012-1393-1.

White, A. B., D. J. Gottas, E. T. Strem, F. M. Ralph, and P. J. Neiman, 2002: An automated brightband height detection algorithm for use with Doppler radar spectral moments. *J. Atmos. Oceanic Technol.,* **19,** 687–697, doi:10.1175/1520-0426(2002)019<0687:AABHDA>2.0.CO;2.

Yin, J. H., 2005: A consistent poleward shift of the storm tracks in simulations of 21st century climate. *Geophys. Res. Lett.,* **32,** L18701, doi:10.1029/2005GL023684.

Zhao, M., I. M. Held, S.-J. Lin, and G. A. Vecchi, 2009: Simulations of global hurricane climatology, interannual variability, and response to global warming using a 50-km resolution GCM. *J. Climate,* **22,** 6653–6678, doi:10.1175/2009JCLI3049.1.

Zhu, Y., and R. E. Newell, 1994: Atmospheric rivers and bombs. *Geophys. Res. Lett.,* **21,** 1999–2002, doi:10.1029/94GL01710.